Supporting information

Effect of cation substitution on pseudocapacitive performance of spinel cobaltite MCo_2O_4 (M = Mn, Ni, Cu, and Co)

Shude Liu[a], Dixing Ni[b], Hai-Feng Li[c], Seong Chan Jun*[,a], Kwun Nam Hui*[,c], Chu-Ying Ouyang*[,b]

[a]School of Mechanical Engineering, Yonsei University, Seoul 120-749, South Korea

[b]Department of Physics, Jiangxi Normal University, Nanchang, 330022, China

[c]Institute of Applied Physics and Materials Engineering, University of Macau, Avenida da Universidade, Taipa, Macau, China.

*Corresponding author's E-mail: scj@yonsei.ac.kr

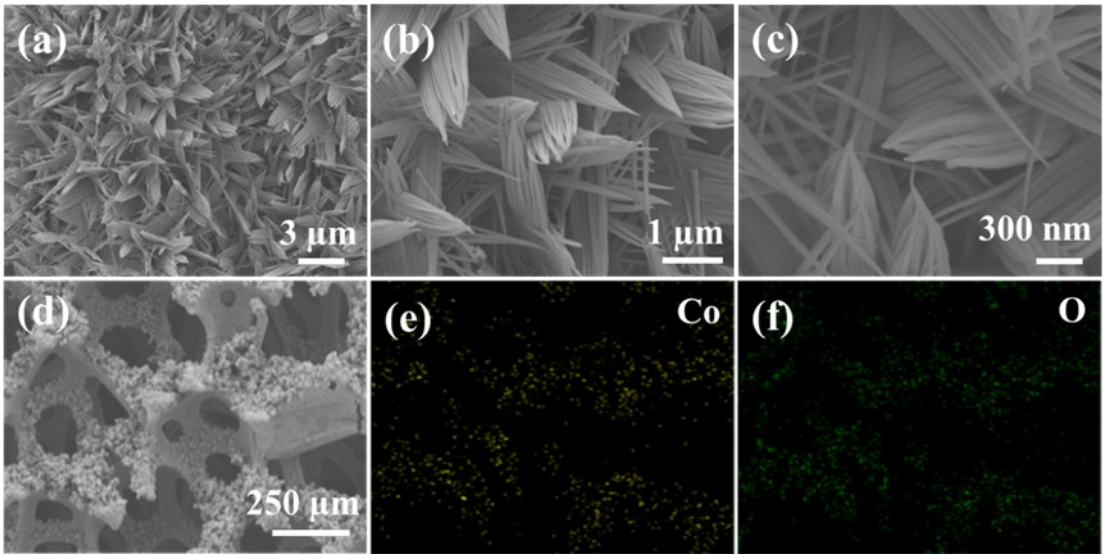

Fig. S1. (a–d) Field emission scanning electron microscopy images of Co_3O_4 nanowires at different magnifications; and (e, f) the corresponding EDS elemental mappings measured from Fig. S1d.

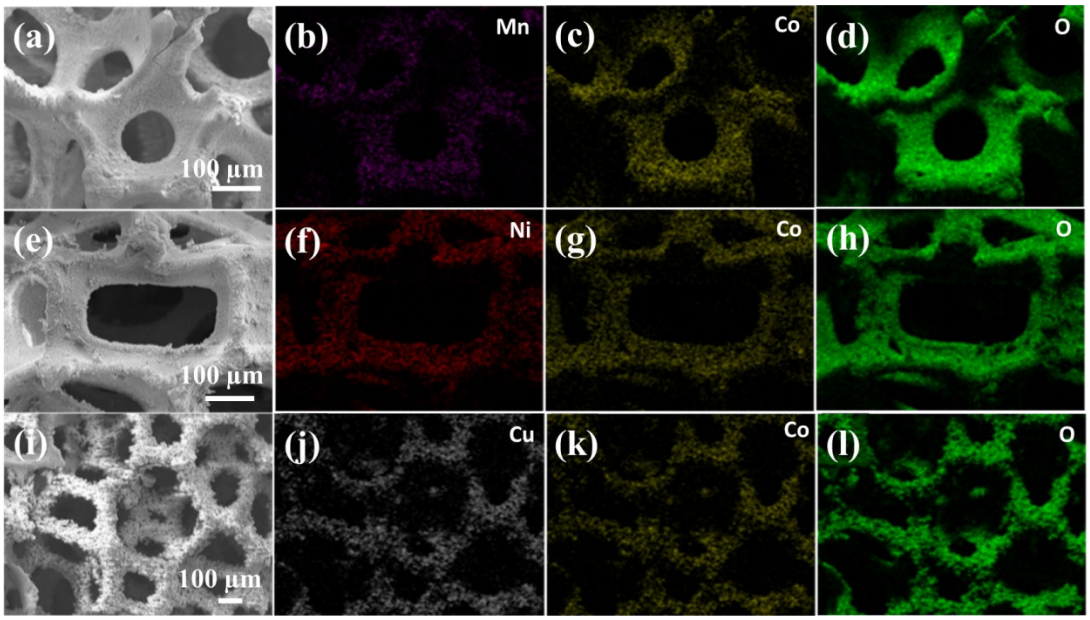

Fig. S2. Field emission scanning electron microscopy images and the corresponding EDS elemental mappings recorded from (a–d) $MnCo_2O_4$, (e–h) $NiCo_2O_4$, and (i–l) $CuCo_2O_4$ nanowires.

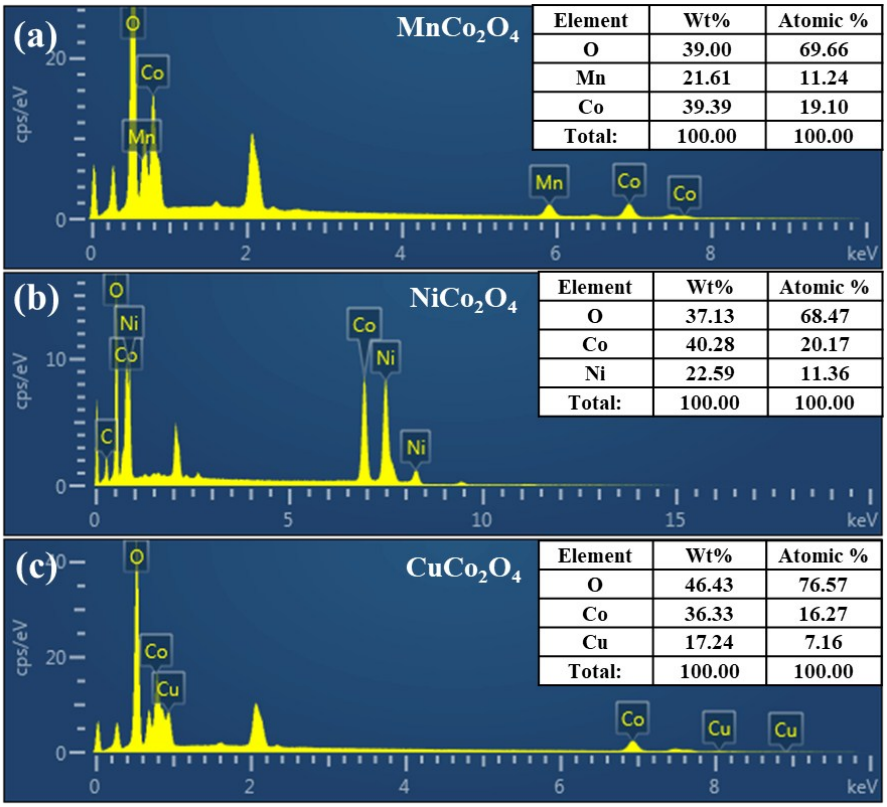

Fig. S3. EDX spectra of the synthesized $MnCo_2O_4$ (a), $NiCo_2O_4$ (b), and $CuCo_2O_4$ (c); the insets show the atomic ratio of Co/M ((i.e., Mn, Ni, and Cu)) by EDX analysis.

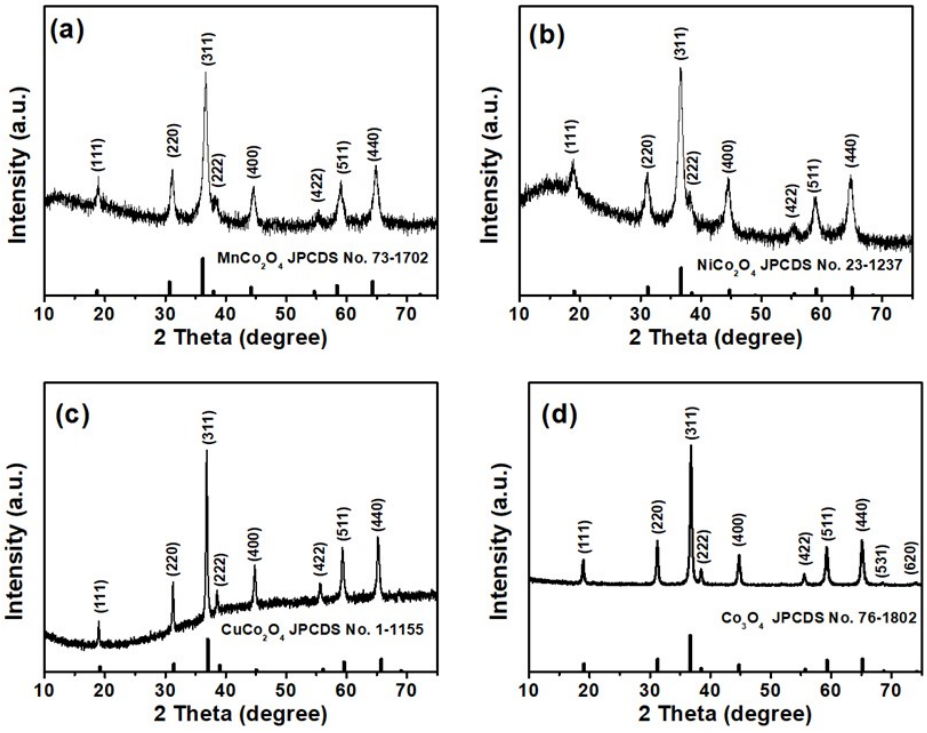

Fig. S4. X-ray diffraction patterns of (a) $MnCo_2O_4$, (b) $NiCo_2O_4$, (c) $CuCo_2O_4$, and (d) Co_3O_4 nanowires.

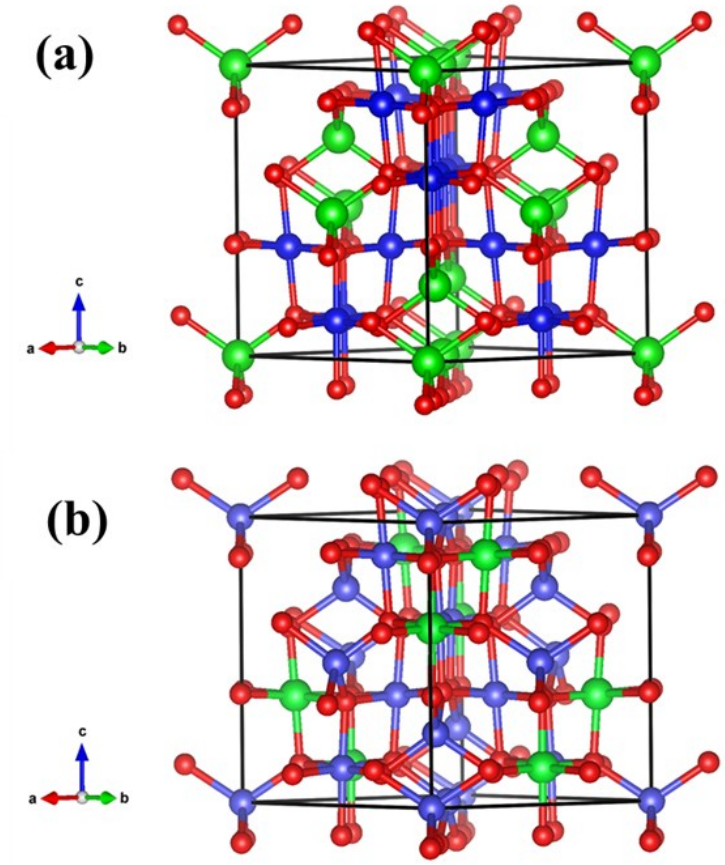

Fig. S5. The ball-and-stick model of (a) normal and (b) inverse spinel MCo_2O_4 (M=Cu, Ni, Mn). The green, blue and red spheres are M (M= Cu, Ni, Mn), Co, and O atoms, respectively.

Fig. S5 presents the normal and inverse spinel structures of MCo_2O_4 (M = Mn, Ni, Cu, and Co). In a conventional unit cell of the spinel structure, O atoms are arranged in a face centered cubic lattice, and there are tetrahedral (8a) sites and octahedral (16d) sites available for the cations. If M atoms occupy the 8a sites and Co atoms occupy the 16d sites, then the structure is named normal spinel. Conversely, if M atoms occupy half of the 16d sites, while Co atoms occupy the 8a sites and the left half of the 16d sites, then structure is named inverse spinel. Due to the different octahedral and tetrahedral crystal fields, the degeneration of the 3d orbital is completely different. Therefore, in order to study the electronic structure of the MCo_2O_4 spinel, the cation occupation in the spinel structure should be considered first.

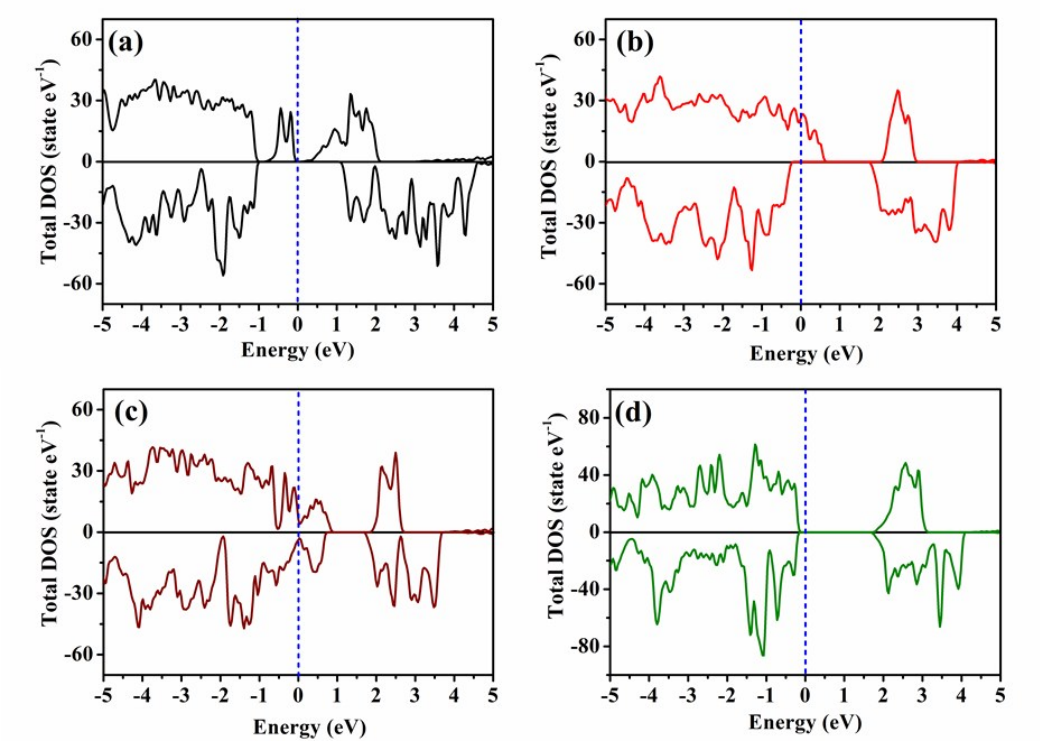

Fig. S6. The total density of states of MCo_2O_4 (M = Ni, Ni, Cu, Co). Spin up and spin down are separated with black and red colors, respectively. The Fermi level is aligned to 0 eV.

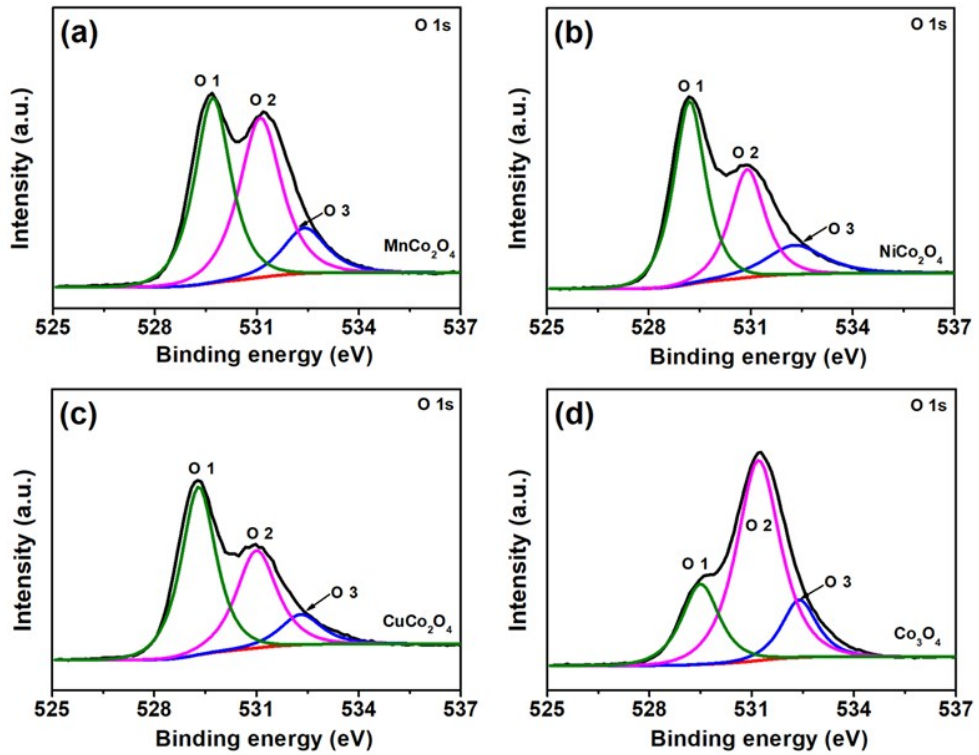

Fig. S7. High-resolution O 1s spectra of (a) $MnCo_2O_4$, (b) $NiCo_2O_4$, (c) $CuCo_2O_4$, and (d) Co_3O_4 nanowires.

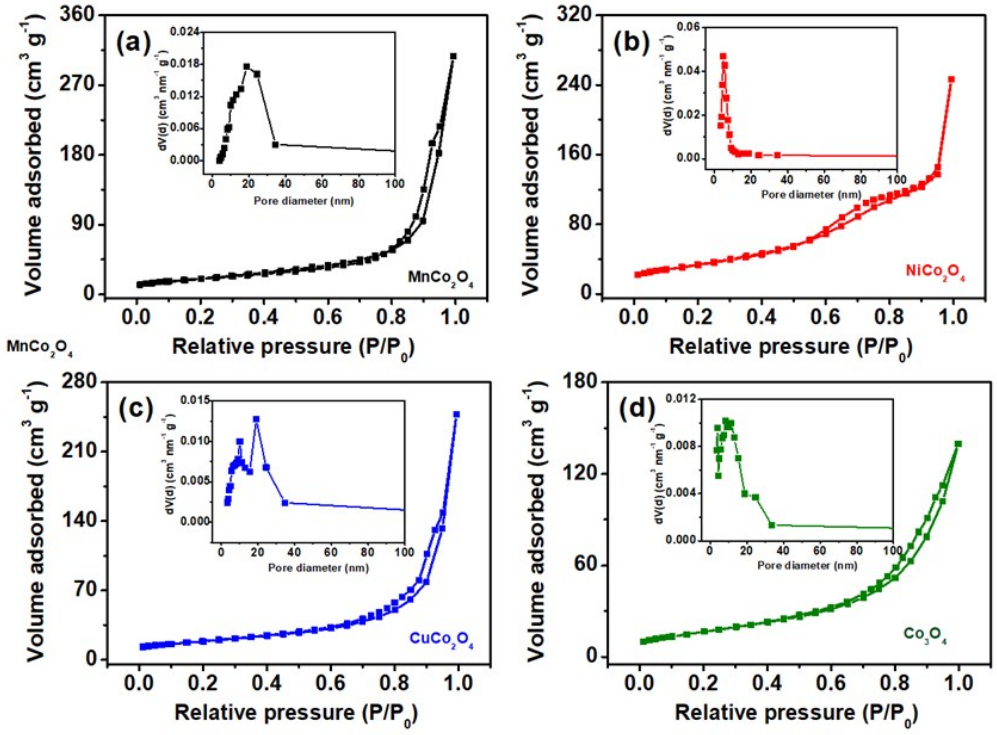

Fig. S8. The nitrogen adsorption–desorption isotherms of the mesoporous MCo_2O_4 (Mn, Ni, Cu, Co) nanowires. The inset shows the corresponding Barrett-Joyner-Halenda pore size distribution plot.

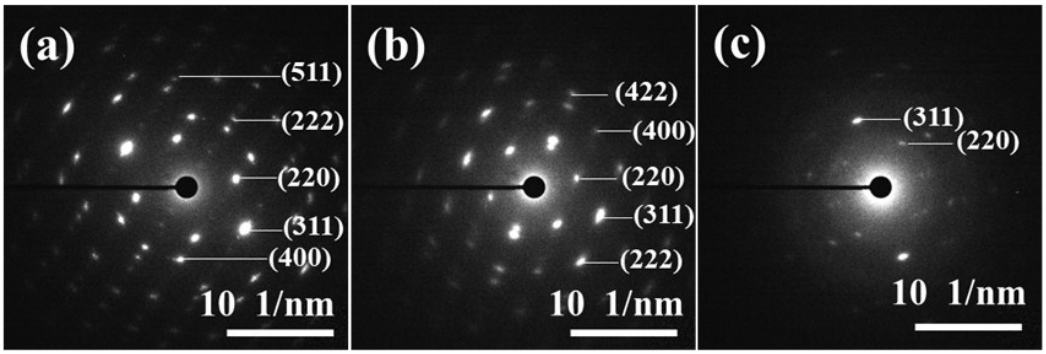

Fig. S9. Selected area electron diffraction patterns of (a) $MnCo_2O_4$, (b) $NiCo_2O_4$, and (c) $CuCo_2O_4$ nanowires.

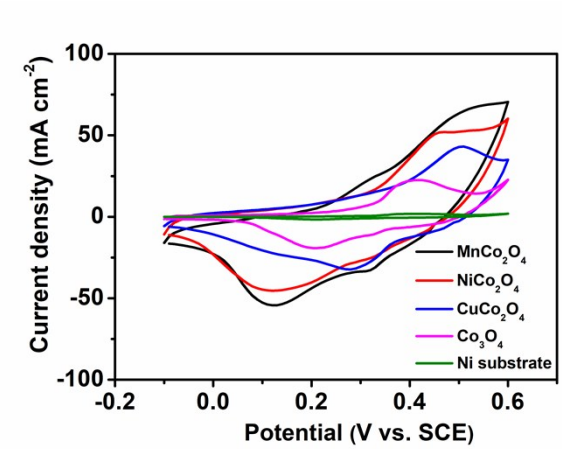

Fig. S10. Comparison of CV curves of $MnCo_2O_4$, $NiCo_2O_4$, $CuCo_2O_4$, Co_3O_4, and NF electrodes obtained at a scan rate of 10 mV s^{-1}.

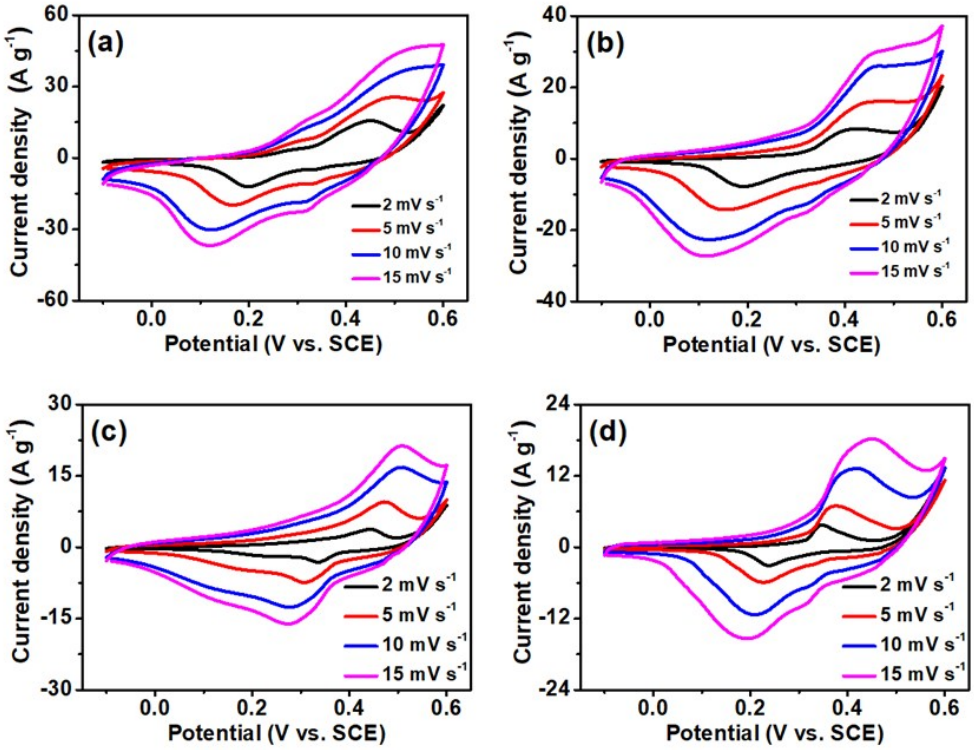

Fig. S11. CV curves of the (a) $MnCo_2O_4$, (b) $NiCo_2O_4$, (c) $CuCo_2O_4$, and (d) Co_3O_4 electrodes obtained at different scan rates ranging from 2 to 15 mV s^{-1}.

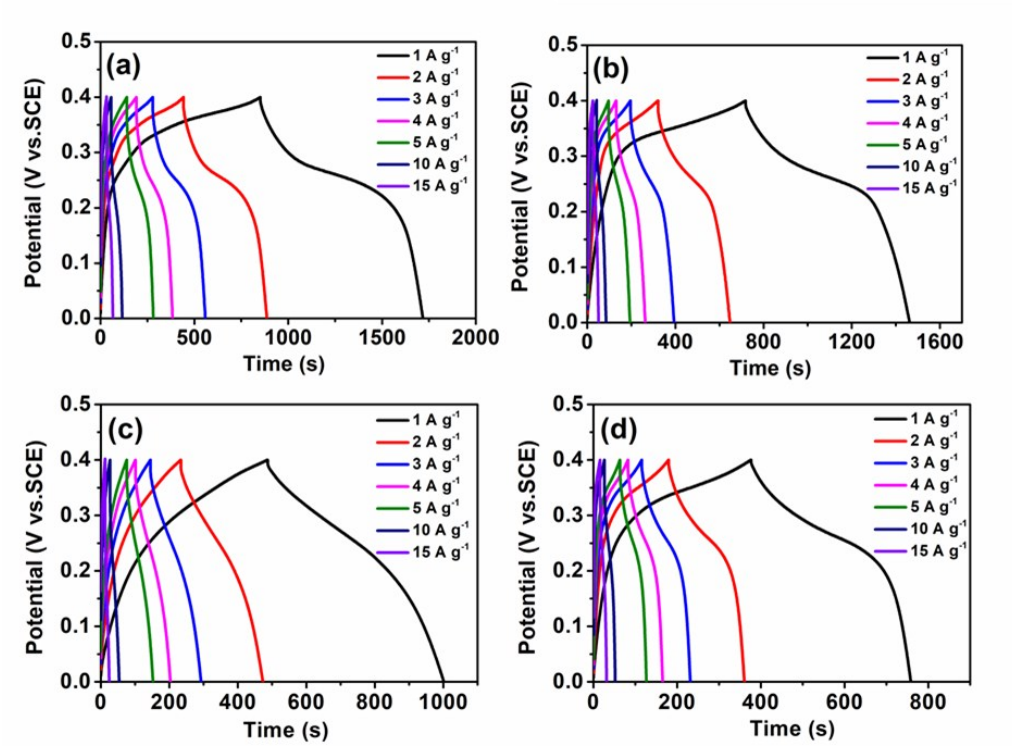

Fig. S12. GCD curves of (a) $MnCo_2O_4$, (b) $NiCo_2O_4$, (c) $CuCo_2O_4$, and (d) Co_3O_4 electrodes obtained at different current densities of 1–15 A g^{-1}.

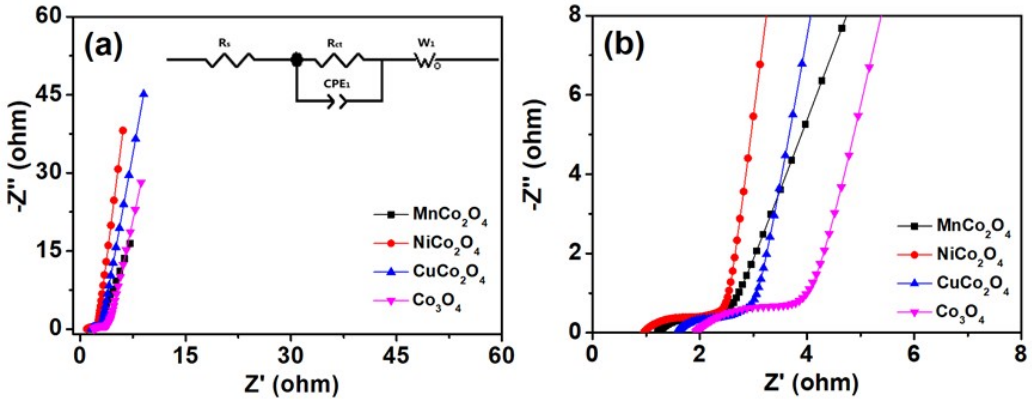

Fig. S13. EIS curves of MCo_2O_4 (Mn, Ni, Cu, Co) electrodes; the inset is the equivalent circuit.

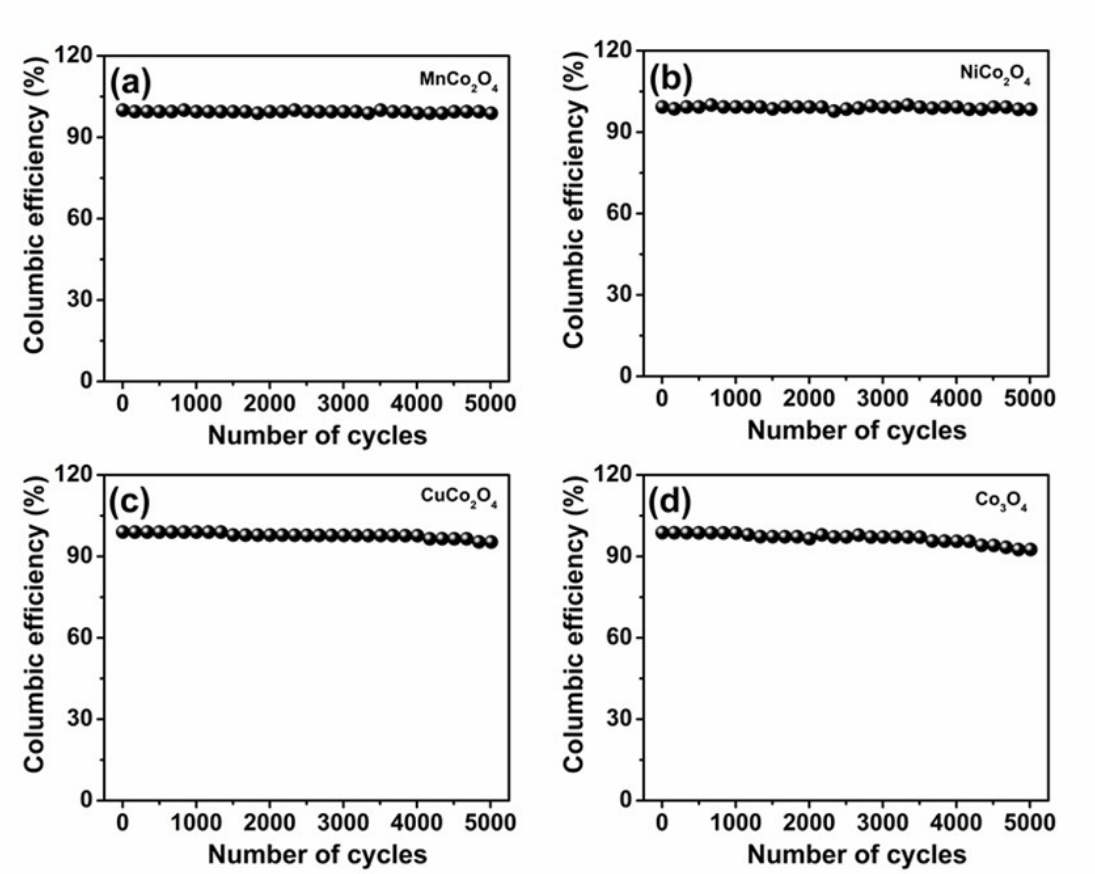

Fig. S14. Coulombic efficiencies of (a) $MnCo_2O_4$, (b) $NiCo_2O_4$, (c) $CuCo_2O_4$, and (d) Co_3O_4 electrodes during cycling tests.

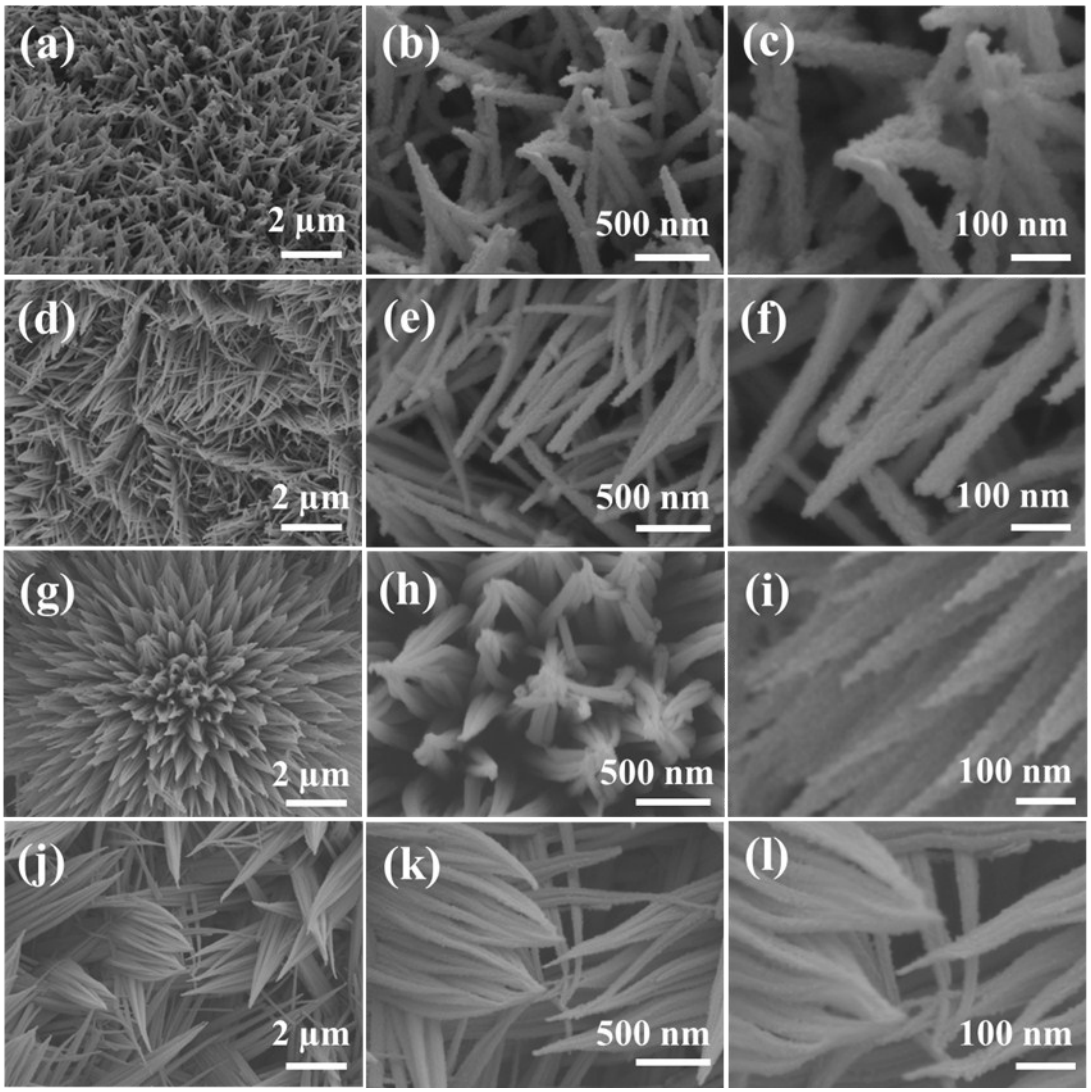

Fig. S15. Field emission scanning electron microscopy images of (a–c) $MnCo_2O_4$, (d–f) $NiCo_2O_4$, (g–i) $CuCo_2O_4$, and (j–l) Co_3O_4 nanowires at different magnifications after cycling tests.

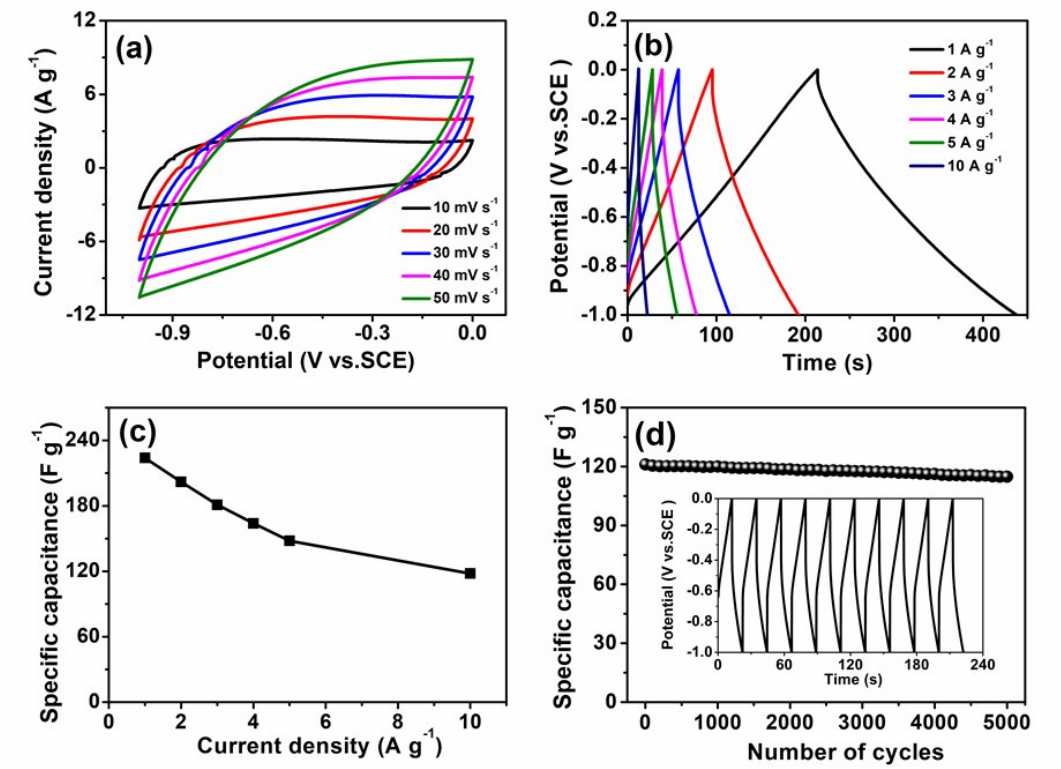

Fig. S16. Electrochemical performance of the AC/NF electrode for supercapacitors: (a) CV curves at various scan rates of 10–50 mV s^{-1}; (b) GCD curves at various current densities of 1–10 A g^{-1}; (c) the specific capacitance at different current densities; (d) cycling performance at a current density of 10 A g^{-1}, the inset of Fig. S15 is the GCD curves in the last ten cycles.

The electrochemical performance of the AC/NF electrode was measured in a three-electrode cell using 1 M KOH as electrolyte (Fig. S15). Fig. S15a presents the CV curves performed at various scan rates of 10–50 mV s^{-1}, which exhibit a quasi-rectangular shape, implying ideal capacitive behavior. Fig. S15b shows the GCD measurements conducted at a voltage ranging from −1–0 V vs. SCE at various current densities of 1–10 A g^{-1}. The specific capacitance calculated from the discharge curves delivers a high specific capacitance of 224 F g^{-1} at 1 A g^{-1}, and remains at 121 F g^{-1} for 10 A g^{-1} (Fig. S15c). The cycle performance of the as-synthesized AC/NF electrode was evaluated at a current density of 10 A g^{-1} (Fig. S15d). The AC/NF electrode exhibits excellent long-term stability with high capacitance retention (94.9%) after 5000 cycles.

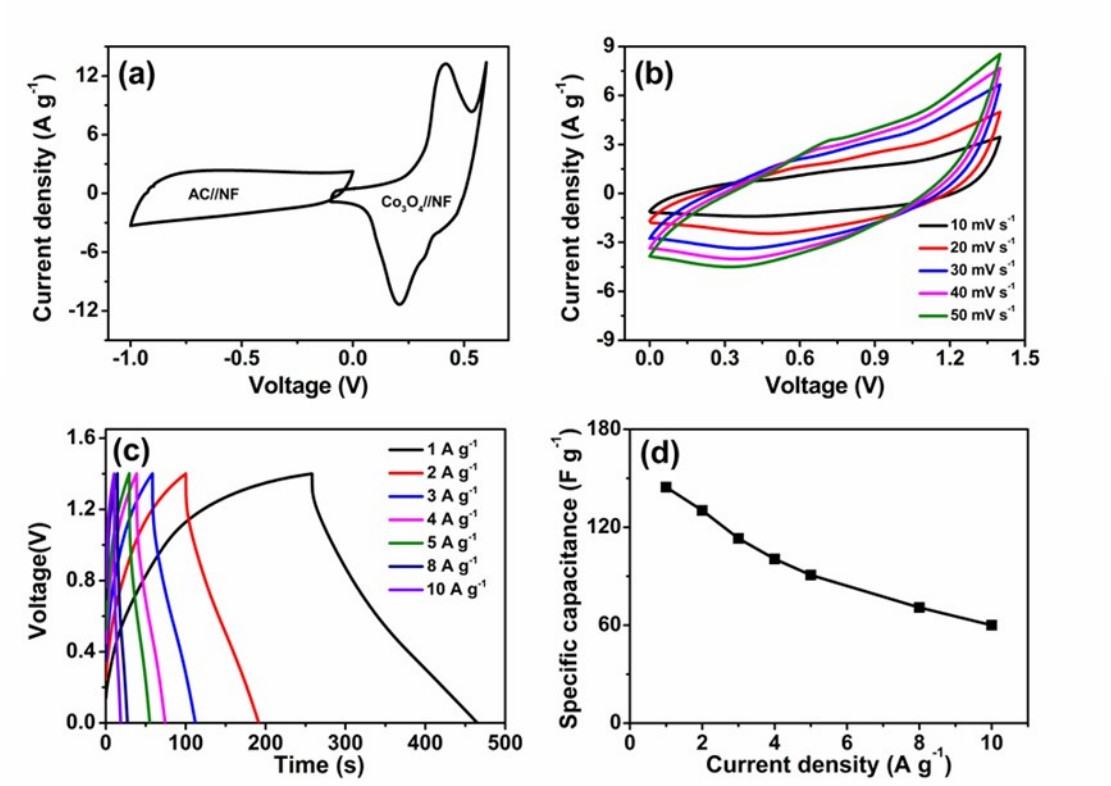

Fig. S17. Electrochemical properties of the Co_3O_4/NF//AC/NF device: (a) Comparison of CV curves of Co_3O_4/NF and AC//NF electrodes at 10 mV s^{-1}; (b) CV curves at various sweep rates ranging from 10–50 mV s^{-1}; (c) GCD curves with different current densities ranging from 1–10 A g^{-1}; (d) Specific capacitance at different current densities.

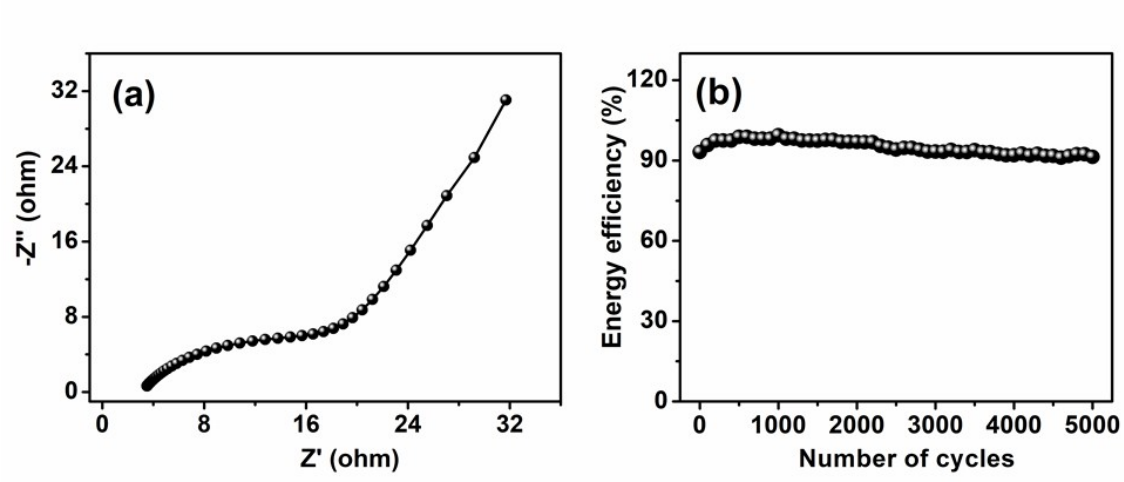

Fig. S18. (a) Impedance Nyquist plot and (b) the Coulombic efficiency in the whole cycling process for the assembled $MnCo_2O_4$/NF//AC/NF device.

Table S1. The calculated free energies F (in eV) of the MCo_2O_4 (M = Cu, Ni, Mn, Co) spinel and inverse-spinel

Free Energy (eV)	$CuCo_2O_4$	$NiCo_2O_4$	$MnCo_2O_4$	Co_3O_4
Normal spinel	-303.15 eV	-315.91 eV	-362.63 eV	-333.87 eV
Inverse spinel	-305.01 eV	-316.09 eV	-365.47 eV	

Table S2. The calculated magnetic moment of the transition metal atoms in the normal spinel and inverse-spinel (lowest energy case) structures

MOM (μ_B)	$CuCo_2O_4$	$NiCo_2O_4$	$MnCo_2O_4$	Co_3O_4
Normal spinel	Cu: 0	Ni: 2.0	Mn: 5.0	Co^{tet}: 3.0
	Co: 0	Co: 0	Co: 0	Co^{oct}: 0
Inverse spinel	Cu: 0	Ni: 1.0	Mn: 4.0	
	Co^{tet}: 3.0	Co^{tet}: 3.0	Co^{tet}: 3.0	
	Co^{oct}: 0	Co^{oct}: 0	Co^{oct}: 0	

Table S3. The calculated lattice parameter of the transition metal atoms in the normal spinel and inverse-spinel structures

Lattice constant (Å)		$CuCo_2O_4$	$NiCo_2O_4$	$MnCo_2O_4$	Co_3O_4
Normal spinel	*a*/*b*/*c*	8.14 8.07 8.14	8.26 8.04 8.06	8.28	8.15
Inverse spinel	*a*	8.25	8.26	8.25	
	b	8.22	8.12	8.25	
	c	8.25	8.17	8.56	

Table S1 presents the calculated free energy F of the MCo_2O_4 (M = Cu, Ni, Mn, Co) spinel and inverse-spinel, which is the sum of the calculated ground state energy and the configurational entropy term (–T·S) at the temperature of sample preparation (623 K) during the post-annealing process. Since all samples are in solid state phases, the PV term is not considered. As for the normal spinel structure, no cation disordering occurs and therefore the configurational entropy is zero. Conversely, for the inverse spinel, cation disordering occurs in the 16d sites. The configurational entropy can be expressed as:

$$S = k_B \ln \Omega = k_B \ln(C_{16}^{8})$$

The sample preparation temperature is 623 K, and therefore the evaluated entropy contribution to the free energy is -0.51 eV for all inverse spinel structures. For Co_3O_4, normal and inverse spinel structures are identical. As for the $MnCo_2O_4$, $NiCo_2O_4$, and $CuCo_2O_4$ inverse spinel cases, different M/Co distribution patterns are considered. The distribution patterns with their corresponding lowest ground state energies and lattice parameters are calculated, as presented in Tables S2-3. Clearly, the inverse spinel structures have lower free energies compared with that of the corresponding normal spinel structures for all ternary MCo_2O_4 cases. The results indicate that the inverse spinel structures are thermodynamically more favorable than the normal spinel structures and therefore all the prepared samples should be inverse spinel. The electronic structures of the ternary MCo_2O_4 are calculated based on inverse spinel structures.

Table S4. Comparison of the maximum C_s of reported cobalt-derived composites as pseudocapacitor electrode materials and the present work.			
Materials	Preparation method	C_s (current density/scan rate)	Ref.
$MnCo_2O_4$ nanoflakes	Hydrothermal method followed by a calcination process	1487 F g^{-1} (1 A g^{-1})	S[1]
$MnCo_2O_4$ nanosheets	Electrodeposition process coupled with a calcination process	290 F g^{-1} (mV s^{-1})	S[2]
$CoMn_2O_4$ nanowires	Hydrothermal method followed by a calcination process	2108 F g^{-1} (1 A g^{-1})	S[3]
$MnCo_2O_4$ nanoparticles@RGO	Hydrothermal method followed by a calcination process	334 F g^{-1} (1 A g^{-1})	S[4]
Flower-like C@$MnCo_2O_4$ nanopetals	Hydrothermal method followed by a calcination process	728.4 F g^{-1} (1 A g^{-1})	S[5]
$MnCo_2O_{4.5}$ nanoneedles/carbon aerogel	Hydrothermal method followed by a calcination process	380 F g^{-1} (0.2 A g^{-1})	S[6]
$NiCo_2O_4$@CNT/CNT films	Co-precipitation coupled with a calcination process	1590 F g^{-1} (0.5 A g^{-1})	S[7]
$NiCo_2O_4$@$NiWO_4$ core–shell nanowires	Hydrothermal method followed by a calcination process	1384 F g^{-1} (1 A g^{-1})	S[8]
$CuCo_2O_4$/$MnCo_2O_4$ heterostructures	Hydrothermal method followed by a calcination process	1216 F g^{-1} (1 A g^{-1})	S[9]
$NiCo_2O_4$ nanoflakes/$MnCo_2O_4$ nanoparticles	Hydrothermal method followed by a calcination process	1100 F g^{-1} (1 A g^{-1})	S[10]

Table S5. Representative fitted EIS parameters based on the experimental impedance spectra.

Materials	Fitted equivalent circuit elements						
	R_s (Ω)	R_{ct} (Ω)	CPE_T	CPE_P	W_R	W_T	W_P
$MnCo_2O_4$	1.201	0.704	0.027	0.729	1.812	1.057	0.413
$NiCo_2O_4$	0.946	0.946	0.020	0.674	1.811	0.620	0.470
$CuCo_2O_4$	1.573	1.353	0.009	0.760	10.45	2.089	0.446
Co_3O_4	1.913	2.137	0.043	0.612	0.295	0.098	0.449

Note: R_s is the combinational resistance of the ionic resistance of electrolyte, intrinsic resistance of substrate, and contact resistance at the active material/current collector interface; R_{ct} is the charge transfer resistance; C_1 is double-layer capacitance; CPE is constant phase element; and W is the Warburg resistance.

Table S6. Refined room temperature structural parameters of $MnCo_2O_4$ as well as the calculated shortest bond lengths (Å) and the goodness of fit.

$MnCo_2O_4$ (cubic, space group *Fd-3m* (NO.227), Z = 8)					
a = b = c (Å)			8.1440(20)	8.1440(20)	8.1440(20)
α, β, γ(◦)			90	90	90
Atom	Site	x	y	z	B ($Å^2$)
Mn	8b	0.3750	0.3750	0.3750	3.34(17)
Co	16c	0.0000	0.0000	0.0000	2.84(15)
O	32e	0.2446(4)	0.2446(4)	0.2446(4)	2.37(21)
Shortest Mn-Mn: 3.5265(1) Å					
Shortest Co-Co: 2.8793(1) Å					
Shortest Mn-Co: 3.3763(1) Å					
Shortest Mn-O: 1.8384(1) Å					
Shortest Co-O: 1.9930(1) Å					
R_B = 2.70, R_F = 2.66, and χ^2 = 2.39					

Table S7. Refined room temperature structural parameters of $NiCo_2O_4$ as well as the calculated shortest bond lengths (Å) and the goodness of fit.

$NiCo_2O_4$ (cubic, space group *Fd-3m* (NO.227), Z = 8)

a = b = c (Å)			8.1207(10)	8.1207(10)	8.1207(10)
α, β, γ(◦)			90	90	90
Atom	Site	x	y	z	B ($Å^2$)
Ni	8b	0.3750	0.3750	0.3750	4.43(9)
Co	16c	0.0000	0.0000	0.0000	3.06(6)
O	32e	0.2442(4)	0.2442(4)	0.2442(4)	1.93(6)
Shortest Ni-Ni: 3.5165(1) Å					
Shortest Co-Co: 2.8712(1) Å					
Shortest Ni-Co: 3.3668(1) Å					
Shortest Ni-O: 1.8398(1) Å					
Shortest Co-O: 1.9943(1) Å					
R_B = 5.1, R_F = 5.78, and χ^2 = 2.39					

Table S8. Refined room temperature structural parameters of $CuCo_2O_4$ as well as the calculated shortest bond lengths (Å) and the goodness of fit.

$CuCo_2O_4$ (cubic, space group *Fd-3m* (NO.227), Z = 8)					
a = b = c (Å)			8.0731(10)	8.0731(10)	8.0731(10)
α, β, γ(◦)			90	90	90
Atom	Site	x	y	z	B (Å^2)
Cu	8b	0.3750	0.3750	0.3750	3.23(19)
Co	16c	0.0000	0.0000	0.0000	1.57(15)
O	32e	0.2422(4)	0.2422(3)	0.2422(3)	2.25(25)
Shortest Cu-Cu: 3.4958(1) Å					
Shortest Co-Co: 2.8543(1) Å					
Shortest Cu-Co: 3.3469(1) Å					
Shortest Cu-O: 1.8555(1) Å					
Shortest Co-O: 1.9581(1) Å					
R_B = 8.54, R_F = 6.95, and χ^2 = 2.76					

Table S9. Refined room temperature structural parameters of Co_3O_4 as well as the calculated shortest bond lengths (Å) and the goodness of fit.

Co_3O_4 (cubic, space group *Fd-3m* (NO.227), Z = 8)					
a = b = c (Å)			8.0994(7)	8.0994(7)	8.0994(7)
α, β, γ(◦)			90	90	90
Atom	Site	x	y	z	B ($Å^2$)
Co1	8b	0.3750	0.3750	0.3750	2.65(8)
Co2	16c	0.0000	0.0000	0.0000	1.97(5)
O	32e	0.2378(1)	0.2378(1)	0.2378(1)	1.76(12)
Shortest Co1-Co1: 3.5071(1) Å					
Shortest Co2-Co2: 2.8636(1) Å					
Shortest Co1-Co2: 3.3578(1) Å					
Shortest Co1-O: 1.9247(1) Å					
Shortest Co2-O: 1.9311(1) Å					
R_B =4.56, R_F = 4.07, and χ^2 = 2.93					

References

S1. A. K. Mondal, D. Su, S. Chen, A. Ung, H. S. Kim and G. Wang, Chem. Eur. J., 2015, **21**, 1526-1532.

S2. S. Sahoo, K. K. Naik and C. S. Rout, Nanotechnology, 2015, **26**, 455401.

S3. Y. Xu, X. Wang, C. An, Y. Wang, L. Jiao and H. Yuan, J. Mater. Chem. A, 2014, **2**, 16480-16488.

S4. Y. Yuan, H. Bi, G. He, J. Zhu and H. Chen, Chemistry Letters, 2013, **43**, 83-85.

S5. L. Li, F. He, S. Gai, S. Zhang, P. Gao, M. Zhang, Y. Chen and P. Yang, CrystEngComm, 2014, **16**, 9873-9881.

S6. P. Hao, Z. Zhao, L. Li, C.-C. Tuan, H. Li, Y. Sang, H. Jiang, C. Wong and H. Liu, Nanoscale, 2015, **7**, 14401-14412.

S7. P. Wu, S. Cheng, M. Yao, L. Yang, Y. Zhu, P. Liu, O. Xing, J. Zhou, M. Wang and H. Luo, Adv. Funct. Mater., 2017, **27**, 1702160.

S8. S. Chen, G. Yang, Y. Jia and H. Zheng, J. Mater. Chem. A, 2017, **5**, 1028-1034.

S9. S. Liu, K. San Hui, K. N. Hui, J. M. Yun and K. H. Kim, J. Mater. Chem. A, 2016, **4**, 8061-8071.

S10. Y. Zhai, H. Mao, P. Liu, X. Ren, L. Xu and Y. Qian, J. Mater. Chem. A, 2015, **3**, 16142-16149.